2-D Wavelet-Based Spectra with Application in Analysis of Geophysical Images

ORIETTA NICOLIS

Dept. of Information Technology and Mathematical Methods

V.le Marconi 5, 24044 Dalmine BG I, Italy

CLAUDIO GARUTTI

Dept. of Information Engineering

Via Gradenigo 6/A, 35131 Padova, Italy

BRANI VIDAKOVIC

Georgia Institute of Technology

Atlanta, GA 30332-0205, USA

Abstract

We propose a wavelet-based spectral method for estimating the (directional) Hurst parameter in isotropic and anisotropic non-stationary fractional Gaussian fields. The method can be applied to self-similar images and, in general, to d-dimensional data that scale. In the application part, we consider denoising of 2-D fractional Brownian fields and the classification of the clouds/temperature

satellite images. In the first application, we use Bayesian inference calibrated by information from the wavelet-spectral domain to separate the signal, in this case the 2-D Brownian field, and the noise. For the classification of geophysical images we first estimate directional Hurst exponents and use them as an input to standard machine learning algorithms.

KEY WORDS: Scaling, Wavelets, Self-similarity, 2D wavelet spectra.

1 Introduction

It is more the rule than the exception that high frequency data collected in real-life experiments, scale in a regular fashion. This scaling is manifested as the "propagation of energy" when observations are inspected at different scales/frequencies, and its regularity is often labeled as ubiquitous or omnipresent. Examples are numerous: high frequency bio-responses, atmospheric data, micro-economic indices, internet data, etc. In many scenarios involving analysis of such data, standard statistical modeling techniques are simply not applicable.

The methodology used to analyze scaling is based on analysis of autocovariances. The covariance dynamics in the domain of original data corresponds to the "energy" scaling in the frequency or scale domains. The term "energy" connotates the squared coefficients in frequency/scale representations of signal and images. Standardly accepted measure of regular scaling is Hurst exponent which can be connected with measures of regularity, dimension, and fractality in signals and images.

Many strategies for assessing the Hurst exponent exist. This assessment can be done in the domain of the original measurements or in some transformed domain (usually scale/frequency domains such as Fourier or wavelet). From the statistical point of view the Hurst exponent could be an informative summary of data and it is often the case that standard statistical techniques are applied not on the data directly, but on their scaling exponents (classification, regression, statistical design).

The literature on the topic is vast (Beran, 1994; Chan and Wood, 2000; Constantine and Hall, 1994; *et al.*, 1995; Mandelbrot and Van Ness, 1968; Pesquet-Popescu, 1999a,b; Pipiras, 2004, 2005; Taqqu *et al.*, 1997). Most of the published research concerns the scaling in one-dimensional data. The theoretical models there are well understood, the estimation and simulation methodology is conceptually and calculatingly straightforward, and univariate high frequency signals that scale are abundant. The definition of scaling in higher dimensions is more complex since multiple formulations are possible. If the scaling is spatial, various directions and choices of neighborhoods are possible, which leads to the possibility of defining various anisotropies. Also, the computational complexity of estimation and simulation methods is higher. However, in geophysical, medical, and other applications the scaling analysis of images and higher-dimensional objects is critically important.

This paper introduces a version of wavelet-based spectra for images and d-dimensional data. The definition of such spectra is quite natural and a few ex-

amples of its use are scattered in the literature (Heneghan *et al.*, 1996; Parra *et al.*, 2003). However, a formal definition and systematic analysis of such spectra was not provided. In addition, the existing applications concern mainly isotropic images.

The idea behind the definition of 2-D wavelet spectra is the following: since the tensor-product wavelet multiresolution analysis of d dimensional data comprises of $2^d - 1$ detail spaces, with each space containing the hierarchy of subspaces with nested dyadic resolutions, it is quite natural to assess the energy scaling in each hierarchy. This leads to $2^d - 1$ concurrent power spectra describing a single d-dimensional data set. For example, multiresolution analysis of images leads to three detail spaces described as "horizontal", "vertical" or "diagonal," depending on the selection of the decomposing 2-D wavelet, or equivalently, the order of applications of high- and low-pass wavelet filters on the rows and columns of 2-D objects. Each of the three directional detail spaces contains a nested hierarchy of submatrices corresponding to image details at different scales and each leads to a distinctive power spectra.

The paper is organized as follows. In the Section 2 we discuss theoretical background necessary for describing self-similarity and scaling in d dimensions. In Section 3 we define the wavelet based directional spectra and discuss some of its properties. Section 4 provides simulational and comparison study in which a noisy 2-D fBm is filtered using properly calibrated Bayes rules. In this section a real-life application of the proposed methodology is discussed: classification of

satellite images with respect to time of their acquisition. In Section 5 we provide conclusions and delineate some possible directions for future research.

2 Background

In this section we review the most popular statistical model for data that regularly scale, the fractional Brownian motion. In one dimension, this process is a unique Gaussian self-similar process with stationary increments. We also briefly discuss multidimensional wavelet domains since the spectrum will be defined there.

2.1 Fractional Brownian motion and extensions

The *fractional Brownian motion* (fBm) is one of the most popular models for modeling self-similar phenomena. It is a Gaussian, zero mean, non-stationary stochastic process, originally proposed by Mandelbrot and Van Ness (1968). This process is indexed by self-similarity parameter H, also known as Hurst exponent. In one-dimensional case the fBm process, denoted by $\{B_H(t), t \in \mathbb{R}\}$, is characterized by its covariance structure

$$R_{B_H}(t,s) = E\{B_H(t)B_H(s)\} = \frac{\sigma_H^2}{2}\left[|t|^{2H} + |s|^{2H} - |t-s|^{2H}\right], \qquad (1)$$

where $\sigma_H^2 = \Gamma(1-2H)\frac{\cos(\pi H)}{\pi H}$. This process possesses a $1/f$ spectrum (Flandrin, 1989) given by

$$S_{B_H}(\omega) \propto \frac{1}{|\omega|^{2H+1}}. \qquad (2)$$

As it can be seen from (1), the fBm is a non stationary process ($R_{B_H}(t,s)$ is not a function of $|t-s|$), but it has stationary increments. In addition, the fBm is a *self-similar process*, that is, for all $a>0$ it satisfies $B_H(at) \overset{d}{=} a^H B_H(t)$, where $\overset{d}{=}$ denotes the equality in distribution.

These properties can be extended to any dimension. Unlike the 1-D case the generalization of fBm to higher dimensions is not unique. A simple generalization to a 2-D surface is the *fractional Brownian field* (fBf). The 2-D *fractional Brownian field* is a Gaussian, zero mean, random field $B_H(\mathbf{u})$, where $\mathbf{u}$ denotes the position in a selected domain, usually $[0,1]\times[0,1]$. Then, the autocorrelation function is

$$R_{B_H}(\mathbf{u},\mathbf{v}) = E\left[B_H(\mathbf{u})B_H(\mathbf{v})\right] = \frac{\sigma_H^2}{2}\left(\|\mathbf{u}\|^{2H} + \|\mathbf{v}\|^{2H} + \|\mathbf{u}-\mathbf{v}\|^{2H}\right), \quad (3)$$

where $0<H<1$ and $\|\cdot\|$ is the usual Euclidean norm in $\mathbb{R}^2$. The increments of the *2-D* fBf represent a stationary, zero mean Gaussian random fields. Because of isotropy, the variance of the increments depends only on the distance $\Delta\mathbf{u}$, so $E\left[|\Delta B_H|^2\right] \propto \Delta\mathbf{u}^H$. The average power spectrum of an isotropic fBf is given by

$$S(\boldsymbol{\omega}) \propto \|\boldsymbol{\omega}\|^{-2H-2}, \quad (4)$$

or coordinatewise by

$$S(\omega_x,\omega_y) \propto \frac{1}{(\omega_x^2+\omega_y^2)^{H+1}}.$$

The self-similarity property can be extended to random fields with stationary increments. Let $B_H(\mathbf{u})$, $\mathbf{u}\in\mathbb{R}^2$, be a continuous-space random field. It is called self-similar with parameter $H>0$ if for all $a>0$ one has $B_H(a\mathbf{u}) \overset{d}{=} a^H B_H(\mathbf{u})$,

where $\stackrel{d}{=}$ means the equality of all finite-dimensional probability distributions. The extension of the fBf to d dimensional case is straightforward and the exponent $-2H-2$ in do not (4) is replaced by $-2H-d$. (see Reed *et al.*, 1995).

Many generalizations have been proposed for defining anisotropic Gaussian random fields. Bonami and Estrade (2003) defined an anisotropic fractional Brownian field, with stationary increments, by considering a spectral density of the form

$$S(\boldsymbol{\omega}) \propto \|\boldsymbol{\omega}\|^{-2H(\boldsymbol{\omega})-2},$$

where $H(\boldsymbol{\omega}) \in (0,1)$ is an even function which depends on the direction $\frac{\boldsymbol{\omega}}{|\boldsymbol{\omega}|}$ of R^2. Popescu and Vehel (2002) introduced anisotropic by linear spatial transforms of an isotropic fractional field. Some other generalizations are Kamont, 1996; Wu and Xiao, 2005, Peltier and Levy, 1996; and Benassi et al., 1997.

2.2 Wavelets

Wavelets are the building blocks of wavelet transforms the same way that the functions e^{inx} are the building blocks of the ordinary Fourier transform. But in contrast to sines and cosines, wavelets can be supported on an arbitrarily small closed interval. Basics on wavelets can be found in many texts, monographs, and papers at many different levels of exposition. The interested reader should consult monographs by Daubechies (1992), Vidakovic (1999), among others.

In 2D (or higher dimensions) wavelets provide an appropriate tool for analyzing self-similar objects and in particular, fractional Gaussian fields. The *energy*

preservation in orthogonal wavelet analysis allows for defining wavelet spectra in a manner similar to that in the Fourier domains. Operationally, the traditional 2D wavelet transforms are constructed through the translations and the dyadic scaling of a product of univariate wavelets and scaling functions,

$$\begin{aligned} \phi(u_x, u_y) &= \phi(u_x) \cdot \phi(u_y) \\ \psi^h(u_x, u_y) &= \phi(u_x) \cdot \psi(u_y) \\ \psi^v(u_x, u_y) &= \psi(u_x) \cdot \phi(u_y) \\ \psi^d(u_x, u_y) &= \psi(u_x) \cdot \psi(u_y), \end{aligned} \tag{5}$$

which is known as *separable* 2D wavelets. The symbols h, v, d in (5) stand for horizontal, vertical and diagonal directions, respectively, and describe the ability of atoms in (5) to emphasize features in these three directions. Any function $f \in L_2(\mathbb{R}^2)$ can be represented as

$$f(\mathbf{u}) = \sum_{\mathbf{k}} c_{j_0,\mathbf{k}} \phi_{j_0,\mathbf{k}}(\mathbf{u}) + \sum_{j \geq j_0} \sum_{\mathbf{k}} \sum_{i} d^i_{j,k_1,k_2} \psi^i_{j,\mathbf{k}}(\mathbf{u}) \tag{6}$$

where $\mathbf{u} = (u_x, u_y) \in \mathbb{R}^2$, $i \in \{h, v, d\}$, $\mathbf{k} = (k_1, k_2) \in Z^2$, and

$$\begin{aligned} \phi_{j,\mathbf{k}}(\mathbf{u}) &= 2^j \phi(2^j u_x - k_1, 2^j u_y - k_2) \\ \psi^i_{j,\mathbf{k}}(\mathbf{u}) &= 2^j \psi^i(2^j u_x - k_1, 2^j u_y - k_2). \end{aligned}$$

for $i = h, v, d$. The decomposition in (6) can be extended to an arbitrary function

$f \in L_2(\mathbb{R}^d)$,

$$\begin{aligned} f(\mathbf{u}) &= \sum_{\mathbf{k}} c_{j_0,\mathbf{k}} \phi_{j_0,\mathbf{k}}(\mathbf{u}) \\ &\quad + \sum_{j \geq j_0} \sum_{\mathbf{k}} \sum_{i=1}^{2^d-1} d^i_{j,\mathbf{k}} \psi^i_{j,\mathbf{k}}(\mathbf{u}), \end{aligned} \tag{7}$$

where $\mathbf{k} = (k_1, \ldots, k_d) \in Z^d$, $\mathbf{u} = (u_1, \ldots, u_d) \in \mathbb{R}^d$, and

$$\begin{aligned} \phi_{j;\mathbf{k}}(\mathbf{u}) &= 2^{jd/2} \prod_{i=1}^{d} \phi(2^j u_i - k_i) \\ \psi^l_{j;\mathbf{k}}(\mathbf{u}) &= 2^{jd/2} \prod_{i=1}^{d} \xi(2^j u_i - k_i) \\ &\quad \text{with } \xi = \phi \text{ or } \psi, \text{ but not all } \xi = \phi. \end{aligned}$$

The index l corresponds to one of $2^d - 1$ possible directions. The d-dimensional wavelet spectra will be defined using the wavelet coefficients in (7), namely $2^d - 1$ nested detail spaces with coefficients $d^i_{j,\mathbf{k}}$, along the scale index j.

3 2D Wavelet Spectra of fBm

Time-frequency representations are indispensable tool in analysis of the signals and images. The spectra in such representations describes distribution of energies in the signal/image along frequencies of scales. Various definitions of spectra exist, depending on the signal representation. Orthogonal discrete wavelets are "energy preserving," and as such, suitable for defining the spectra. Wavelets and wavelet based spectra have been instrumental in analysis of self-similarity (Flandrin, 1989, 1992; Doukhan *et al.*, 2003; Wornell, 1995). The definition of wavelet

spectra involves average "energies" in the detail spaces of wavelet-transformed signal.

Suppose that 1-D signal y of length n has wavelet decomposition $d = Wy = (c_{j_0}, d_{j_0}, d_{j_0+1}, \ldots, d_j)$, where j_0 is a fixed level smaller than $j = \log_2 n - 1$, c_{j_0} are scaling, and d_j's are vectors of detail coefficients. The wavelet spectra is defined as

$$S(j) = \log_2 \left(\overline{d_j^2} \right)$$

where $\overline{d_j^2}$ is an average of squared components in vector d_j.

In the 2D case three different hierarchies constitute detail spaces and the natural definition of wavelet spectra involves the three power spectra corresponding to the hierarchies. Since the detail hierarchies are characterized by their direction (horizontal, vertical and diagonal), the spectra will be sensitive in assessing the energy content and dissipation along the angles of 0, $\pi/2$, and $\pi/4$.

Consider a 2-D fBm process, $B_H(\mathbf{u})$, that is standard model for self-similar random fields. For this process the wavelet coefficients are given by

$$d^i_{j,\mathbf{k}} = 2^j \int B_H(\mathbf{u}) \psi^i(2^j \mathbf{u} - \mathbf{k}) d\mathbf{u}, \tag{8}$$

where the integral is taken over $\mathbb{R}^2$ and $i = h, v$ or d. The detail coefficients are random variables with zero mean and variance

$$E\left[\left| d^i_{j,\mathbf{k}} \right|^2 \right] = 2^{2j} \iint \psi^i \left(2^j \mathbf{u} - \mathbf{k} \right) \psi^i \left(2^j \mathbf{v} - \mathbf{k} \right) E\left[B_H(\mathbf{u}) B_H(\mathbf{v}) \right] d\mathbf{u} d\mathbf{v}, \tag{9}$$

(Heneghan *et al.*, 1996). From the definition of ψ^h and ψ^v in (5), the integrand in (9) is symmetric and the variances of the wavelet coefficients coincide for these

two directions, that is

$$E\left[\left|d^h_{j,\mathbf{k}}\right|^2\right] = E\left[\left|d^v_{j,\mathbf{k}}\right|^2\right]. \tag{10}$$

These two variances differ from the variance of the wavelet coefficients from the diagonal hierarchy. From (9) one can derive

$$E\left[\left|d^i_{j,\mathbf{k}}\right|^2\right] = \frac{\sigma_H^2}{2} V_{\psi^i} 2^{-(2H+2)j}, \tag{11}$$

where

$$V_{\psi^i} = \iint \psi^i(\mathbf{p}+\mathbf{q}) \cdot \psi^i(\mathbf{q}) \left|\mathbf{p}\right|^{2H} d\mathbf{p} d\mathbf{q}$$

depends only on wavelets ψ^i and H, but not on the scale j. The derivation is given in the Appendix I.

By applying the logarithm to both sides of Eq. (11) the following equation is obtained

$$\log_2 E\left[\left|d^i_{j,\mathbf{k}}\right|^2\right] = -(2H+2)j + C_i, \tag{12}$$

where

$$C_i = \log_2 \frac{\sigma_H^2}{2} V_{\psi^i}(H). \tag{13}$$

The Hurst coefficients of a 2D fBm field can be estimated from the slope in the linear equation given in (12). The empirical counterpart of (12) is a regression defined on pairs

$$\left(j, \log_2 \overline{\left|d^i_{j,\mathbf{k}}\right|^2}\right), \quad i = h, v, d, \tag{14}$$

where $\overline{\left|d^i_{j,\mathbf{k}}\right|^2}$ is an empirical counterpart of $E\left[\left|d^i_{j,\mathbf{k}}\right|^2\right]$. The sample mean in (13) can be replaced by sample median or any other location estimation to produce

more robust estimators of the spectra. Also the regression should be weighted since the variances in the levels are not equal anymore. Veich and Abry (1999) discuss the bias of estimators in (14) and the method to correct it.

Anisotropic generalization is straightforward; the parameter H in the above equations (8-14) can depend on the direction i and may be replaced by H_i. Given the wavelet ψ, the intercept C_i in (12), is uniquely determined by H, and initial energy, σ_H^2. Thus, if H and C_i vary independently, a novel, wavelet-specific class of anisotropic self-similar random fields can be defined. Few examples are provided for the isotropic and anisotropic cases. Figure 1(a) depicts simulated isotropic fractional Brownian field with $H = 0.3$. Its 2D wavelet spectra based on the *Symmlet 4* filter, shown in Figure 1(b), demonstrates the estimation process is consistent. The resulting estimates are $\hat{H}_h = 0.295$, $\hat{H}_v = 0.298$, and $\hat{H}_d = 0.299$ for the horizontal, vertical and diagonal directions, respectively, which are close to the original simulated value of $H = 0.3$. In order to select the best basis and test performance of wavelet-based estimator, we simulated 1000 fractional Brownian fields with various H and for each field estimated the Hurst parameter in each of the three directions. The averaged wavelet-based estimator was compared with Quadratic Variations (QV) estimator introduced by Istas and Lang (1997). As typical for many wavelet based procedures, the choice of basis is important but not decisive for the results and performance of the estimation algorithm. We comprehensively explored Daubechies, Symmlet and Coiflet families for a range of parameter values (vanishing moments) and the differences found were not sig-

nificant (the Haar basis being an exception). We adopted short filters with different smoothness and symmetry properties such the Daubechies 4, Symmlet 4 and Coiflet 1 (as in Table 1). For comparative purpose we use Symmlet 4 since this filter provides a good compromise of smoothness, locality and near-symmetry. In Table 1 we provide the summary of this experiment. We found that the averaged wavelet-based estimates are close to those obtained by the QV method for isotropic fields simulated with $H = 0.4$ and with $H = 0.6$. These two exponents are selected to represent antipersistency and long memory. Moreover, the wavelet based estimator was more robust when the data are contaminated by noise, even at a low level. For the estimation procedure of the wavelet spectra, we used the Ordinary Least Square (OLS) estimator. We also implemented weighted least squares (WLS) in the spirit of Veitch and Abry (1999). For calculating regression weights we resampled detail spaces to obtain a surrogate sample of logarithms of average level energies. These are further utilized to obtain proper weights via bootstrap variances. The difference between the weighted and the ordinary least squares regression was found to be minimal which was a consequence of typically large sample sizes in image processing. The WLS also substantially increased computational complexity. For example, in the case of $n = 10$ simulated images 512×512 with $H = 0.6$ the OLS gave $\hat{H} = 0.6238$ with a standard deviation of 0.04 while the WLS gave $\hat{H} = 0.6232$ with similar standard deviation.

In the second example we simulated an anisotropic Gaussian random field us-

	$H = 0.4$		$H = 0.6$	
	snr= ∞	snr= 20	snr= ∞	snr= 20
D4	0.3920 (0.042)	0.3828 (0.325)	0.6027 (0.035)	0.5775 (0.340)
S4	0.3968 (0.042)	0.3838 (0.326)	0.6005 (0.033)	0.5766 (0.359)
C1	0.3865 (0.042)	0.3766 (0.041)	0.5917 (0.037)	0.5715 (0.045)
Haar	0.3508 (0.041)	0.3427 (0.040)	0.5554 (0.035)	0.5327 (0.045)
QV	0.3886 (0.016)	0.3365 (0.027)	0.5886 (0.015)	0.2663 (0.086)

Table 1: Means and standard deviations (in brackets) of the estimated Hurst exponents, by the wavelet-based estimators (D4, S4, C1 and Haar) and the QV estimator, evaluated on 1000 simulated random fields with $H = 0.4$ and $H = 0.6$ and length $n = 256 \times 256$, with and without noise in each case.

ing Daubechies 4 wavelet by controlling the scaling of variances in detail spaces. An example of simulated field is given in Figure (2(a). In particular, we considered scaling equivalent to Hurst parameters equal to $H_h = 0.3$, $H_v = 0.8$, and $H_d = 0.5$, for the horizontal, vertical, and diagonal direction, respectively. The 2D wavelet-spectra assessed by a wavelet different than generating (Daub 8) gave the following estimates: $\hat{H}_h = 0.297$, $\hat{H}_v = 0.820$, and $\hat{H}_d = 0.511$ (Figure 2(b)) which are very close to those utilized in the simulation of the field. The goal of this exercise was to produce a specific direcy=tional anisotropy and to check that 2-D spectra consistently estimates the scaling when basis is changed.

In order to show the behavior of the intercepts C_i for each direction, we have simulated $N = 200$ isotropic fractional Brownian fields on a regular grid ($512 \times$

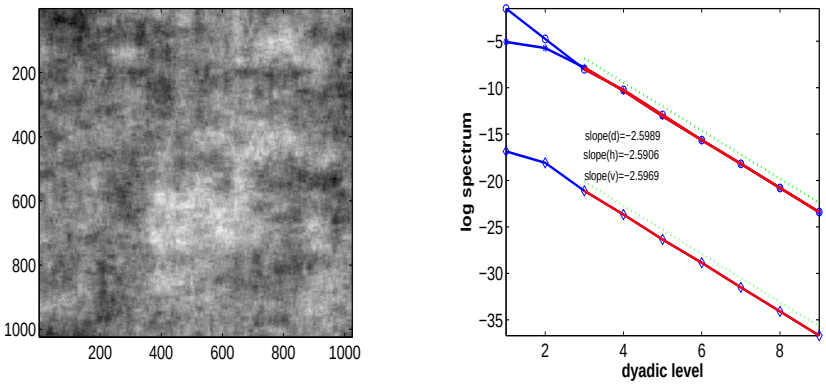

(a) (b)

Figure 1: (a) Isotropic fractional Brownian field with $H = 0.3$; (b) The wavelet spectra of the field in (a) estimated by Symmlet 4.

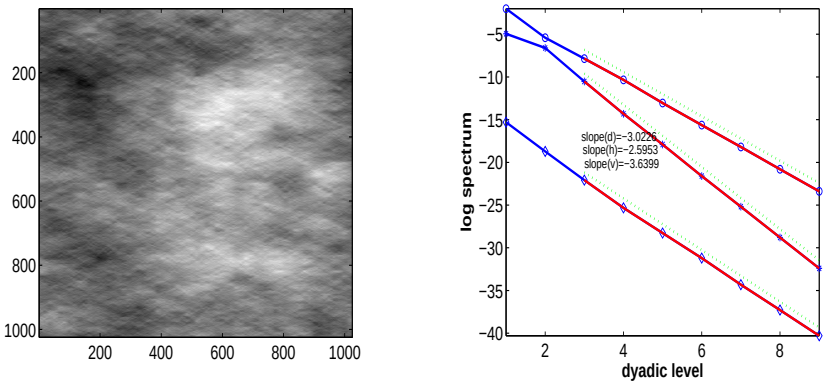

(a) (b)

Figure 2: (a) Gaussian random field with $H_h = 0.3$, $H_v = 0.8$, and $H_d = 0.5$ simulated by Daubechies 4; (b) The 2-D wavelet spectra of the field in (a) estimated by Symmlet 4.

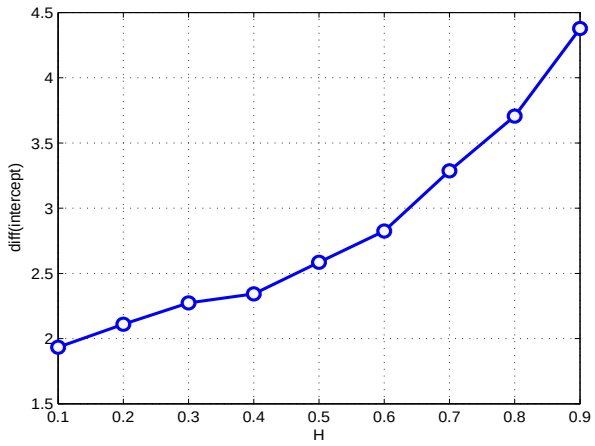

Figure 3: Average differences of the intercepts for horizontal and diagonal directions, $\overline{C}_h - \overline{C}_d$, for different values of parameter H.

512) with parameters H ranging from $H = 0.1$ to $H = 0.9$. Figure 3 plots the average difference of the intercepts for the horizontal and diagonal directions, $\overline{C}_h - \overline{C}_d$. It is evident that the intercept is affected by the value of H: for higher H the estimated difference $\overline{C}_h - \overline{C}_d$ is larger.

The message of this analysis is the following: Even for the isotropic random fields the amount of energy attributed to different directions differs. Note that $C_i = \log_2(\sigma_H^2 V_{\psi^i}) - 1$, where σ_H^2 is the variance of fBm and V_{ψ^i} is given in (24), and precise numerical evaluation of an intercept C_i is possible. Evaluation of C_i's is critical for the simulation of random fields using 2-D wavelets, since it specifies how the total energy should be distributed to the directional subspaces.

4 Applications

In this section we provide two applications in which 2-D wavelet spectra is instrumental. The first application concerns denoising task in which the signal image exhibits scaling. The separation of the signal image and noise is done by Bayesian wavelet filtering calibrated by the properties of the corresponding $2-D$ spectra. The second application involves the statistical task of image classification with 2-D spectra parameters as discriminatory descriptors. In the spirit of a reproducible research all MATLAB codes utilized in these applications are available from the authors on request.

4.1 Bayesian filtering guided by spectral information

In this application we demonstrate how 2D wavelet spectra can be utilized in filtering noisy images in which the "signal" part scales.

Suppose the observed image $\mathbf{y}$ is a convolution of an unknown "true" image $\mathbf{s}$, exhibiting scaling, and a random noise $\mathbf{e}$,

$$\mathbf{y} = \mathbf{s} + \mathbf{e}. \tag{15}$$

It is assumed that the random noise is a matrix of *iid* zero mean Gaussians with standard deviation σ_e and that the "true" image is well modeled by a fractional Brownian motion, with its parameter H not known in advance. In the wavelet domain, expression (15) becomes $d^i_{j\mathbf{k}} = \theta^i_{j\mathbf{k}} + \varepsilon^i_{j\mathbf{k}}$, where $d^i_{j\mathbf{k}}, \theta^i_{j\mathbf{k}}$, and $\varepsilon^i_{j\mathbf{k}}$ are the $(j, \mathbf{k})$ coordinates in the traditional scale/shift wavelet-enumeration of trans-

formed images $\mathbf{y}, \mathbf{s}$ and $\mathbf{e}$, respectively. This model preservation a consequence of linearity and orthogonality of wavelet transforms. In the exposition that follows, we omit the double index $j, \mathbf{k}$ and the direction i, and work with a "typical" wavelet coefficient, d. The conditional distribution of d given θ and σ^2, $[d|\theta, \sigma^2]$, is $\mathcal{N}(\theta, \sigma^2)$. We utilize Bayesian Adaptive Multiscale Shrinkage (BAMS), a technique proposed in Vidakovic and Ruggeri (2001) to statistically estimate wavelet coefficients, corresponding to 2D fBm, using a shrinkage rule in a Bayesian framework.

In BAMS, σ^2 and θ are assumed to be independent random variables. The variance σ^2 is given exponential $\mathcal{E}(\mu)$ prior, while θ is given a mixture prior, as standardly done. The mixture prior consists of a point mass at zero (representing the "parsimony" part) and a double exponential distribution (representing the "spread" part) mixed in proportion $(1-\varepsilon) : \varepsilon$,

$$(1-\varepsilon)\delta_0 + \varepsilon \mathcal{DE}(0, \tau).$$

The resulting Bayes rule is given by:

$$\delta^*(d) = \frac{(1-\epsilon)\, m(d)\, \delta(d)}{(1-\epsilon)\, m(d) + \epsilon\, \mathcal{DE}\left(0, \frac{1}{\sqrt{2\mu}}\right)}, \tag{16}$$

where

$$m(d) = \frac{\tau e^{-|d|/\tau} - \frac{1}{\sqrt{2\mu}} e^{-\sqrt{2\mu}|d|}}{2\tau^2 - 1/\mu}$$

is the predictive distribution of d, and

$$\delta(d) = \frac{\tau(\tau^2 - 1/(2\mu))de^{-|d|/\tau} + \tau^2(e^{-|d|\sqrt{2\mu}} - e^{-|d|/\tau})/\mu}{(\tau^2 - 1/(2\mu))(\tau e^{-|d|/\tau} - (1/\sqrt{2\mu})e^{-|d|\sqrt{2\mu}})}$$

is the corresponding Bayes rule with respect to the squared error loss. The Bayes rule depends on the hyper-parameters ε, τ, and μ. The elicitation of the hyper-parameters is critical for good performance of Bayesian filtering. A variety of default solutions are available, but default choice do not seem to be very suitable in function estimation, since observations can vary tremendously and but to accommodate for possibly very different images and signal-to-noise ratios, a degree of informativeness and/or data dependence should be exploited. The hyper-parameters have been set using Empirical Bayes (EB) arguments, as in Vidakovic and Ruggeri (2001) or Katul *et al.* (2006). The rule in (4.1) is close to a thresholding rule: it heavily shrinks small-in-magnitude arguments while the large arguments are only slightly shrunk.

Having the calibrated rule (4.1), the separation of $\mathbf{s}$ and $\mathbf{e}$ is performed as follows: each wavelet coefficient d is split as

$$d = \delta^*(d) + (d - \delta^*(d)) = \hat{\theta} + \hat{\varepsilon},$$

with $\delta^*(d)$ and $(d - \delta^*(d))$ estimating signal and noise contributions, respectively. All $\hat{\theta} = \delta^*(d)$ form a matrix $\widehat{\boldsymbol{\theta}}_{j,\mathbf{k}}$ which back-transformed to the original image domain gives the estimator of denoised image.

This process of filtering is illustrated in Figures 4, 5, and 6 where we consider a 2-D fBf with Hurst exponent $H = 1/3$ with an addittive Gaussian noise in which the signal-to-noise ratio equal to $snr = 2$. In particular, Fig. 4 (a) show the the 2-D simulated fBf . In order to better show the effect of the noise on the image, we show in panel (b) of Figure 4 the $100-$th row of the simulated image with and

without noise.

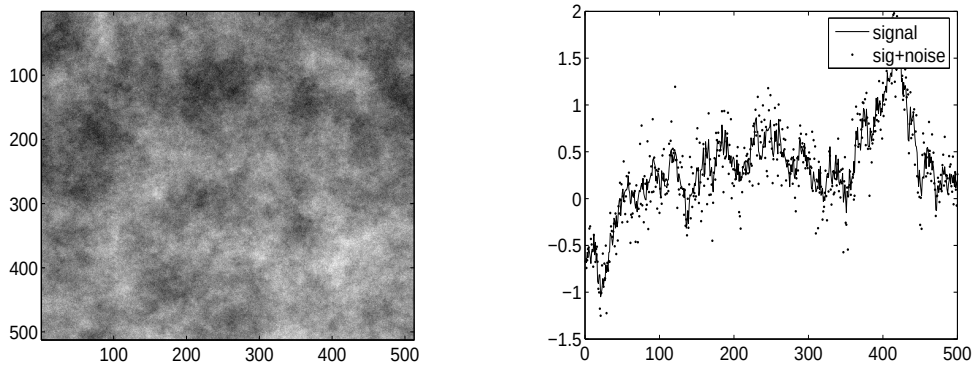

(a) (b)

Figure 4: a) Simulated 2D fBm with $H = 1/3$; (b) Signal of $100-$th and signal with noise.

Figure 5(a) shows the wavelet power spectra for the noisy and denoised images utilizing the *Symmlet 4* wavelet filter. The estimates for H, in each direction, resulting from the slopes of Eq. (12), are $\hat{H}_h = 0.3204$, $\hat{H}_v = 0.3161$, and $\hat{H}_d = 0.2739$, for the horizontal, vertical and diagonal direction, respectively. Note the flattening of directional spectra (black solid lines) of the noisy image. That means that noise which is affecting all scales and all coefficients, has sufficient energy to leave its signature only on finest levels of details (high dyadic levels) where its relative energy compared to that of the signal image is high.

The described filtering procedure based on Bayesian inference rule is able to recover the simulated image since the estimator of H is close to the original and, at the same time, the estimator of the noise is close to a matrix of iid Gaussians.

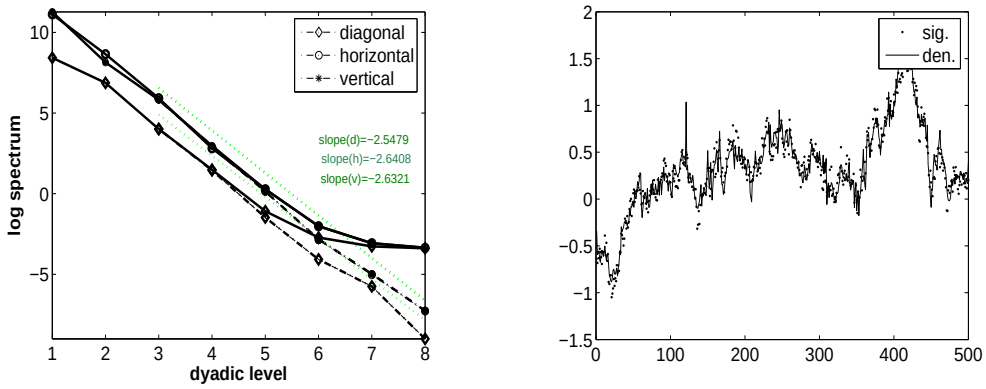

(a) (b)

Figure 5: (a) 2D wavelet-based spectra. Black solid lines depict the directional spectra of the noisy images while the gray lines are "straightened" and correspond to denoised image. (b) Signal of $100-$th row and denoised image.

This is evident from Figure 5(b) and 6. While the panel (b) of Figure 5 shows the result of denoising by comparing the $100-$th row of the original image to the $100-$th row reconstructed image after applying the Bayes rule, the 6 (a) shows the marginal distribution of magnitudes of all residuals. The later suggest that the components have zero-mean and bell-shaped distribution which is consistent with the originally simulated noise. To show that the residuals are not "colored", we selected $100-$th (out of 512) row of the estimated noise matrix. In addition to their marginal Gaussianity, the autocorrelation of components in the $100-$th row is consistent with "whitenes", i.e., no autocorrelations at nonzero lags are significant. The autocorrelations for the first 100 lags are shown in Figure 6 (b).

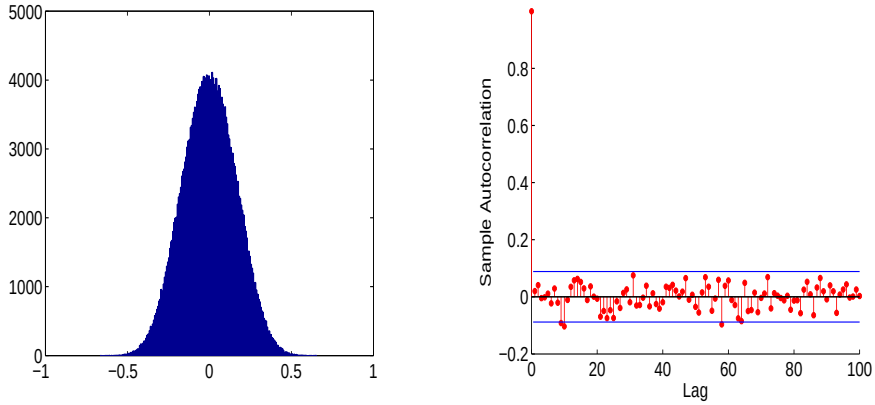

(a) (b)

Figure 6: (a) Histogram of all residuals; (b) Autocorrelation function of $100-$th row in the residual matrix.

4.2 Classification of Cloud/Temperature Maps

In this application we illustrate how the wavelet-based estimators of directional Hurst exponents can be utilized in classification of satellite images. The emphasis here is on discrimination abilities of the Hurst summaries, and not on a solution of a realistic environmental problem. It is straightforward to implement the described analysis in various scientific areas in which 2-D data are instrumental: medical imaging, geoscience, industrial applications, etc.

The source of the data is EUMETSAT (`http://www.eumetsat.int`). EUMETSAT is an intergovernmental organization created through an international convention signed by 17 European Member States. EUMETSAT's Meteosat system is intended primarily to support the National Meteorological Ser-

vices (NMS) of Member States. The NMS in turn distributes the image data to other end-users, notably through the provision of forecasts on television several times a day. In addition to the provision of images of the Earth and its atmosphere every half an hour in three spectral channels (Visible, Infrared and Water Vapour), a range of processed meteorological parameters is produced.

The satellite receives that part of the sun radiation which is reflected by the earth surface or by cloudiness. It is a so-called *window channel* which means that radiation is not significantly absorbed by the gases in the troposphere. The satellite receives radiation which is emitted by the earth and the clouds because of their temperature. Infra Red (IR) images via is window channel (Wavelength 3.9-13.4 microns (μ)) are useful for day and night cloud-mapping and determination of surface temperature. A range of grey shades in the IR channel represent different temperatures of the radiating surface which can either be the earth surface or the cloud tops.

Our data set contains 160 IR satellite images of the Gulf of Guinea (West cost of Africa and South Atlantic Ocean). The images are taken at 3.9 μ IR band for 40 consecutive days (11/1/2006 - 12/10/2006), and subsequently divided into 4 groups according to the hour of their acquisition: (i) night (0:12am), (ii) morning (6:12am), (iii) noon (12:12pm), and (iv) evening (6:12pm). A typical observation (6:12 am, 11/1/06, IR 3.9 μ) is shown in Figure 7.

There are factors, different than geography (terrain), possibly influencing the scaling in the satellite image, such as clouds, wind, temperature level, humidity,

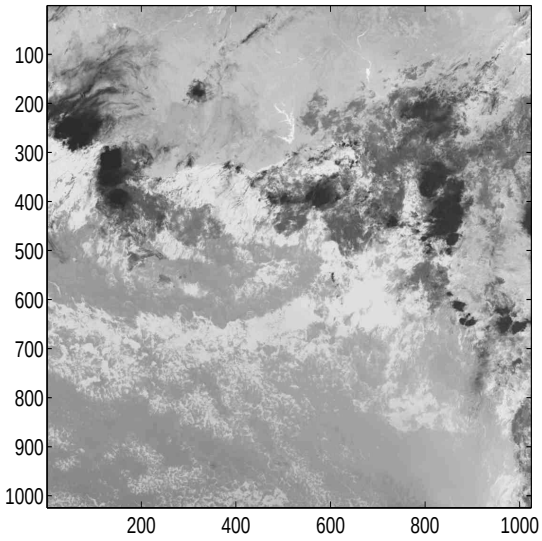

Figure 7: Satelite IR image with wavelength $3.9\ \mu$, taken on November 11, at $06:12am$ (morning group).

etc. These "background conditions" are differently influenced by time of day and exhibit no regular behavior. It natural to base discrimination by global scaling properties of the observed images.

In order to assess the efficacy of Hurst exponents to classify images to groups with different texture characteristic, the following experiment was performed. We randomly selected a portion of the data to fit the classification model and used the reminder of data to test the model. Two scenarios are considered: the first uses 50% of data as a training set and the second 70%. The random sampling of training data was repeated 10000 times, so the prediction errors are averaged over 10000 runs.

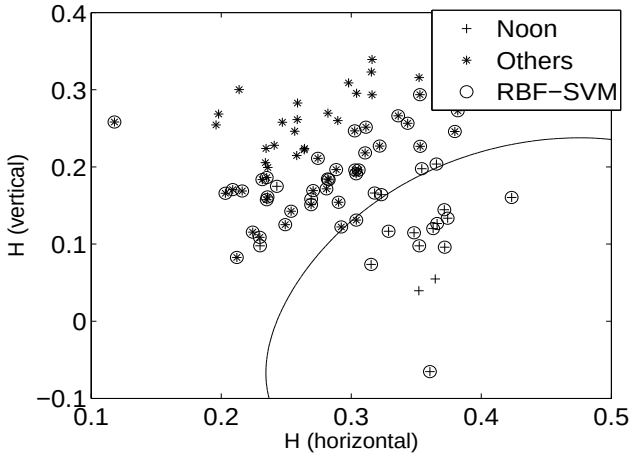

Figure 8: Training set (80 sample) and non linear boundaries by radial bases SVM ($c = 2$). Observation with circles are support vectors.

Several exogenous variables (such temperature, wind, humidity, pressure) at noon are different than the same variables at the other times of the day, we considered only two groups for the classification purpose: the "noon" group and "others" group. For classifying the data we considered several classification procedures: linear, quadratic and SVM (Support Vector Machines) (see Hastie *et al.*, 2001). In Table 2 we provide results obtained with the linear and quadratic classifiers and with SVM with different kernel functions: linear, quadratic, polynomial (with degree $d = 3$), and radial basis (with scaling parameter $c = 2$). Figure 8 shows an example of classification of "noon" and "others" images by the radial basis SVM (with $c = 2$) and in Table 2 we provide some results.

As evidenced by Table 2 the standard linear classifier outperforms all other.

Testing Proportion	Lin,	Quad.	Lin. SVM	Quad. SVM	Poly. SVM	RBF SVM
50%	0.072	0.081	0.085	0.088	0.084	0.086
30%	0.069	0.077	0.086	0.086	0.079	0.084

Table 2: Misclassification errors for some classical classifiers (Lin. and Quad.) and selected SVM methods (Lin. SVM, Quad. SVM, Poly. SVM, and RBF SVM) for 50% and 30% of data used for testing.

This is a consequence of almost perfect linear separation between the "noon" and "others". We also performed classification experiments in which harder-to-separate cases are considered. In these cases, the SVMs were distinctly superior to the linear and quadratic classifiers. For example, in the "evening" and "others" case the error rate was about 15% and in "morning" and "others" about 25%. This later rate was affected by scaling similarities between "morning" and "midnight" images belonging to different classes.

Figure 9 shows a linear classifier based on 50% of data and the testing set consisting of remaining 50%. Only a few observations are misclassified.

On a horizontal-vertical Hurst plane, the *asterisks* correspond to the "noon" group while the *plus* correspond to "others" containing the remainder of the data. The misclassified cases are circled on the graph.

This example shows that in the case of anisotropy the directional spectra can well capture informative anisotropies and produce discriminatory summaries. In

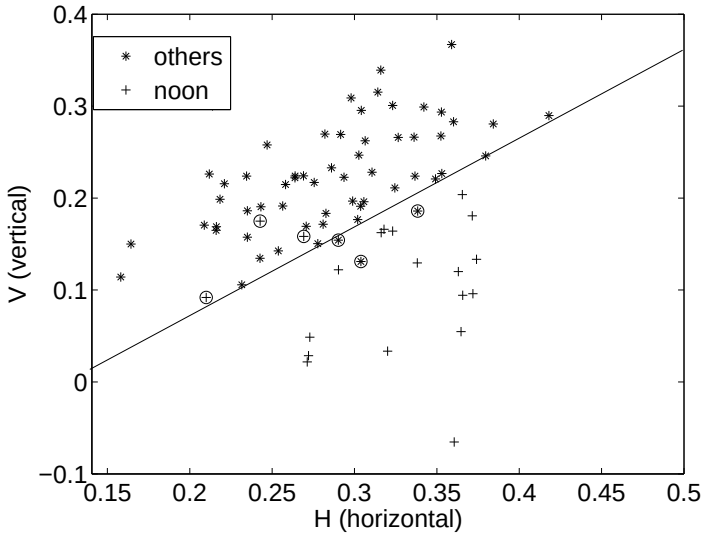

Figure 9: Testing set (based on 50% of data) and linear classifier. The circled observations are misclassified.

particular, the horizontal and vertical directions captured most of significant differences between the groups.

5 Conclusions

We have shown that a 2D wavelet-based spectra, evaluated trough the sample moments of wavelet coefficients, can be used for estimating the Hurst parameter vector in a variety of self-similar random fields. Examples of standard isotropic fractional Brownian fields as well as anisotropic non-stationary Gaussian fields are provided in the context of estimation of their directional Hurst parameters.

The methodology involving statistical models in the wavelet spectral domain has been developed and applied in denoising of composite images in which the "signal part" is self-similar. This is done by considering directional 2D spectra and empirically calibrating a Bayesian shrinkage rule which preserves regular scaling in the estimator of the signal image and assures marginal normality and independence of the residuals. It is interesting that the signal image is a random field itself and this application is in fact a challenging separation of two random fields.

We also utilized the 2D wavelet spectra to classify geophysical images. In particular, we classified clouds/temperature map images to their corresponding groups by a linear discriminator fed by the vector of directional Hurst exponents. The Hurst descriptors have shown to be discriminatory, leading to a classifier with an excellent percentage of correct predictions (91.25%). Further extension of this

methodology to other classes of anisotropic processes is under investigation.

Acknowledgments: This work was done while the first and second authors were visiting the Georgia Institute of Technology. The work of O. Nicolis has been partially supported by Italian Research grants by MIUR (PRIN2004). Support for C. Garutti was provided in part by *Fondazione Ing. Aldo Gini* The work of B. Vidakovic was partially supported by the NSF grant DMS 0004131 at Georgia Tech. The authors are grateful to EUMETSAT, and in particular to Mr Bob Barrett for help about satellite images used in the application part.

Appendix I

The tensor product wavelet transform are standard way of generating $d-$dimensional multiresolution analysis. The atomic function in (5) is such that $\{\psi^i_{j,k_1,k_2} = 2^{\frac{j}{2}}\psi^i\left(2^j u_x - k_1, 2^j u_y - k_2\right)\}$ for each direction i. For a fBm process, $B_H(u_x, u_y)$, the wavelet coefficients are

$$d^i_{j,k_1,k_2} = 2^j \iint B_H(u_x, u_y)\psi^h(2^j u_x - k_1, 2^j u_y - k_2)du_x du_y \qquad (17)$$

By setting $\mathbf{k} = (k_1, k_2)$ and $\mathbf{u} = (u_x, u_y)$, Eq. (17) can be written as

$$d^i_{j,\mathbf{k}} = 2^j \iint B_H(\mathbf{u})\psi^i(2^j\mathbf{u} - \mathbf{k})d\mathbf{u}. \qquad (18)$$

The variance of the detail coefficients $d^i_{j,\mathbf{k}}$ is obtained in a similar way to the continuous wavelet approach described in (Heneghan *et al.*, 1996), is

$$E\left[\left|d^i_{j,\mathbf{k}}\right|^2\right] = 2^{2j}\iint \psi^i\left(2^j\mathbf{u}-\mathbf{k}\right)\psi^i\left(2^j\mathbf{v}-\mathbf{k}\right)E\left[B_H(\mathbf{u})B_H(\mathbf{v})\right]d\mathbf{u}\,d\mathbf{v} \quad (19)$$

Taking into the account the definition of the covariance function for a fBm in 2D, we have

$$\begin{aligned} E\left[\left|d^i_{j,\mathbf{k}}\right|^2\right] &= \frac{\sigma_H^2}{2}2^{2j}\iint \psi^i\left(2^j\mathbf{u}-\mathbf{k}\right)\psi^i\left(2^j\mathbf{v}-\mathbf{k}\right)|\mathbf{u}|^{2H}\,d\mathbf{u}d\mathbf{v} \\ &\quad + \iint \psi^i\left(2^j\mathbf{u}-\mathbf{k}\right)\psi^i\left(2^j\mathbf{v}-\mathbf{k}\right)|\mathbf{v}|^{2H}\,d\mathbf{u}d\mathbf{v} \\ &\quad + \int \psi^i\left(2^j\mathbf{u}-\mathbf{k}\right)\psi^i\left(2^j\mathbf{v}-\mathbf{k}\right)|\mathbf{u}-\mathbf{v}|^{2H}\,d\mathbf{u}d\mathbf{v}. \end{aligned} \quad (20)$$

Since,

$$\int \psi^i\left(2^j\mathbf{u}-\mathbf{k}\right)d\mathbf{u} = \int\left(2^j\mathbf{v}-\mathbf{k}\right)d\mathbf{v} = 0, \quad (21)$$

the variance in (20) can be simplified as

$$E\left[\left|d^i_{j,\mathbf{k}}\right|^2\right] = \frac{\sigma^2}{2}2^{2j}\iint \psi^i\left(2^j\mathbf{u}-\mathbf{k}\right)\psi^i\left(2^j\mathbf{v}-\mathbf{k}\right)|\mathbf{u}-\mathbf{v}|^{2H}\,d\mathbf{u}d\mathbf{v} \quad (22)$$

By substituting $\mathbf{p} = 2^j(\mathbf{u}-\mathbf{v})$ and $\mathbf{q} = 2^j\mathbf{v}-\mathbf{k}$, we obtain:

$$\begin{aligned} E\left[\left|d^i_{j,\mathbf{k}}\right|^2\right] &= \frac{\sigma_H^2}{2}2^{2j}\iint \psi^i\left(\mathbf{p}+\mathbf{q}\right)\psi^i\left(\mathbf{q}\right)2^{-2jH}|\mathbf{p}|^{2H}\,2^{-4j}d\mathbf{p}d\mathbf{q} \\ &= \frac{\sigma_H^2}{2}2^{-j(2H+2)}\iint \psi^i\left(\mathbf{p}+\mathbf{q}\right)\psi^i\left(\mathbf{q}\right)|\mathbf{p}|^{2H}\,d\mathbf{p}d\mathbf{q} \\ &= \frac{\sigma_H^2}{2}V_{\psi^i}2^{-j(2H-2)}, \end{aligned} \quad (23)$$

where V_{ψ^i} denotes

$$\iint \psi^i(\mathbf{p}+\mathbf{q}) \cdot \psi^i(\mathbf{q}) \left|\mathbf{p}\right|^{2H} d\mathbf{p} d\mathbf{q}, \tag{24}$$

an integral depending on wavelet ψ^i and H, but free of the scale j.

$$E\left[\left|d^i_{j,\mathbf{k}}\right|^2\right] = \frac{\sigma_H^2}{2} V_{\psi^i} 2^{-(2H+2)j} \tag{25}$$

By applying logarithm to both ends in (25) the following equation is obtained

$$\log_2 E\left[\left|d^i_{j,\mathbf{k}}\right|^2\right] = -(2H+2)j + C_i,$$

(discussion previously on Section 3).

References

BERAN, J. (1994). *Statistics for Long-Memory Processes*, Volume 61 of Monographs on Statistics and Applied Probability. New York: Chapman & Hall.

BONAMI, A. AND ESTRADE, A. (2003) Anisotropic analysis of some Gaussian models, *Journal of Fourier Anal. and Appl.*, 9, Number 3 (2003) 215–236.

CHAN, G. and WOOD, A. T. A. (2000). Increment-based estimators of fractal dimension for two-dimensional surface data, *Statist. Sinica* 10, 343–376.

CONSTANTINE, A. G. and HALL, P. (1994). Characterizing surface smoothness via estimation of effective fractal dimension, *J. Roy. Statist. Soc. Ser. B* 56, 97–113.

DAUBECHIES, I. (1992). Ten lectures on wavelets, CBMS-NSF Regional Conference Series in Applied Mathematics, 61, SIAM, Philadelphia.

DOUKHAN, P., OPPENHEIM, G., TAQQU, M. S. (2003). *Theory and Applications of Long-Range Dependence*, Birkhauser.

FLANDRIN, P. (1989). On the Spectrum of Fractional Brownian Motions, *IEEE Transaction on Information Theory*, 35, 197–199.

FLANDRIN, P. (1992). Wavelet analysis and synthesis of fractional Brownian motion, *IEEE Transaction on Information Theory*, 38, 910–917.

HENEGHAN, C., LOWEN, S.B., TEICH, M.C. (1996). Two dimensional fractional Brownian motion: wavelet analysis and synthesis. Image Analysis and Interpretation, *Proceedings of the IEEE Southwest Symposium*, 213–217.

KAMONT, A.(1996). On the fractional anisotropic Wiener field, *Probab. Math. Statist.* 16, 85—98.

KATUL, G. G., RUGGERI, F. and VIDAKOVIC, B. (2006). BAMS filtering and applications to denoising ozone concentration measurements, *Journal of Statistical Planning and Inference*, 136, 2395–2405.

MANDELBROT, B. B. and VAN NESS, J. W. (1968). Fractional Brownian Motions, Fractional Noises and Applications, *SIAM Review* 10(4) 422–437.

PARRA, C., IFTEKHARUDDIN, K., and RENDON, T. (2003). Wavelet based estimation of the fractal dimension in fBm images. Presented in the *1st IEEE EMBS conference on Neural Engineering* , March.

PIPIRAS V. (2004). On the usefulness of wavelet-based simulation of fractional Brownian motion, Preprint. Available at http://www.stat.unc.edu/faculty/pipiras/.

PIPIRAS V. (2005). Wavelet-based simulation of fractional Brownian motion revisited. Applied and Computational Harmonic Analysis, 19(1), 49–60.

PESQUET-POPESCU, B. VÉHEL, J. L. (2002) Stochastic Fractal Models for Image Processing, *IEEE Signal Procesing Magazine*, 48-62.

PESQUET-POPESCU, B. (1999). Statistical Properties of the Wavelet Decomposition of Some Non-Gaussian Self-Similar Processes, *invited paper*, *Signal Processing*, 75, 303–322.

PESQUET-POPESCU, B. (1999). Wavelet Packet Analysis of 2D Processes with Stationary Fractional Increments, *IEEE Transactions on Information Theory*, 45(3), 1033–1039.

REED, I. S., LEE, P. C., and TRUONG, T. K. (1995). Spectral representation of fractional Brownian motion in n dimensions and its properties Information Theory, *IEEE Transactions*, 41(5), 1439–1451

TAQQU M. S., TEVEROVSKY V., and WILLINGER, W. (1997). Is network traffic self-similar or multifractal? *Fractals*, 5–63.

VIDAKOVIC B. and RUGGERI F. (2001). BAMS Method: Theory And Simulations, textit-Sankhya, Series B, 63, 234–249.

VIDAKOVIC, B. (1999). *Statistical Modeling by Wavelets,* John Wiley & Sons, New York.

WORNELL, G. (1995). *Signal Processing with Fractals: A Wavelet Based Approach*, Prentice Hall.

WU, D. and XIAO Y. (2005). Geometric properties of the images of fractional Brownian sheets, *J. Fourier Anal. Appl.* To appear.